Toward a Physical Explanation of the Seasonal Dynamics and Thermodynamics of the Gulf of California

P. RIPA

Centro de Investigación Científica y de Educación Superior de Ensenada, Ensenada, Mexico

(Manuscript received 29 January 1996, in final form 3 June 1996)

ABSTRACT

The annual component of the horizontal heat flux $\mathcal{F}^x$ is calculated from the temperature advection by the geostrophic velocity. This estimate of $\mathcal{F}^x$ is in good agreement, in amplitude and phase and as a function of the distance x to the head, with that calculated from the difference between the surface heat flux Q and the local heating, that is, from $\partial\mathcal{F}^x/\partial x = Q - \partial\mathcal{H}/\partial t$, where $\mathcal{H}$ denotes the heat content.

Sea level η variations are well correlated with those of $\mathcal{H}$, while the surface velocity u_{surf} (which can be calculated from the difference of η between both coasts) is well correlated with $\mathcal{F}^x$. The proportionality coefficients between (η, $\mathcal{H}$) and between (u_{surf}, $\mathcal{F}^x$) correspond to what is expected for a dominance of the first baroclinic mode, in spite of the inhomogeneity of the gulf's topography.

A linear one-dimensional two-layer model is enough to reproduce the observations of the transversely averaged (η, $\mathcal{H}$, u_{surf}, $\mathcal{F}^x$) fields at the annual frequency. Most of the dynamics and thermodynamics are controlled by the Pacific Ocean, which excites a baroclinic Kelvin wave at the mouth of the gulf. Wind drag produces a slight slope in η, whereas Q causes a local heating of the upper layer; both surface forcings have a small effect on u_{surf} and $\mathcal{F}^x$.

1. Introduction

The Gulf of California (Fig. 1) attracts the attention of both observationalists and modelers for two main reasons: There is interest in the gulf per se and it also constitutes a good sized basin for the test of mesoscale and climate scale modeling. Many works concentrate on the seasonal variation because it stands out in noisy and sparse datasets. Quite often, statements on the seasonality of a certain field are only qualitative, based on the signature of its variability as a function of the month (e.g., Robles and Marinone 1987; Bray 1988; Marinone and Ripa 1988). In order to better understand the physics of the gulf, more quantitative results are needed, like those obtained through a fit of the data to annual—or annual plus semiannual—harmonics. This type of analysis will be used in this paper; all uncertainty estimates quoted here have to do exclusively with the goodness of the seasonal fit and not with measurement or other errors. This work is then strongly based on three other publications on the seasonal variability of the Gulf of California, which employ a harmonic data analysis: those of Ripa and Marinone (1989), Ripa (1990), and Castro et al. (1994); hereafter denoted by RM89, R90, and CLR94, respectively. The main results of these papers are reviewed next.

In RM89 we worked with hydrographic variables on the Guaymas–Santa Rosalía transect, including both the annual and semiannual frequencies in the analysis. We found a good correlation between the incoming heat flux and the vertical temperature gradient at the surface; namely, $Q \approx \kappa_v[\rho C_p \partial T/\partial z]$ corresponding to $\kappa_v = (3.2 \pm 0.1) \times 10^{-4}$ m^2 s^{-1}. By extending this parameterization of the vertical heat flux $\mathcal{F}^z$, below the surface, calculating its z derivative and adding the rate of change of the heat content $\mathcal{H}$, the horizontal heat flux divergence was computed; that is, $\partial\mathcal{F}^x/\partial x = -\partial\mathcal{H}/\partial t - \partial\mathcal{F}^z/\partial z$. To the dismay of 1D (in the vertical) modelers, it was found that the horizontal divergence of heat flux is as important, or even more important, than the vertical one. Horizontal salt flux divergence was also found to be very important, but at the same time the freshwater balance was seen to be more complicated than the heat balance, because the semiannual salinity signal is not smaller than the annual one. Finally, we also found that the surface elevation at Guaymas is mainly due to the seasonal heating of the water column (isostatic conditions) plus a smaller contribution of the geostrophic tilt, associated with the surface velocity (which had been computed from hydrography).

Sea level and atmospheric pressure data along the coast of the gulf were examined in R90, including both the annual and semiannual frequencies in the analysis.

Corresponding author address: Dr. Pedro Ripa, CICESE, Km 107 Carretera Tijuana-Ensenada, (22800) Ensenada, BC, Mexico.
E-mail: ripa@cicese.mx

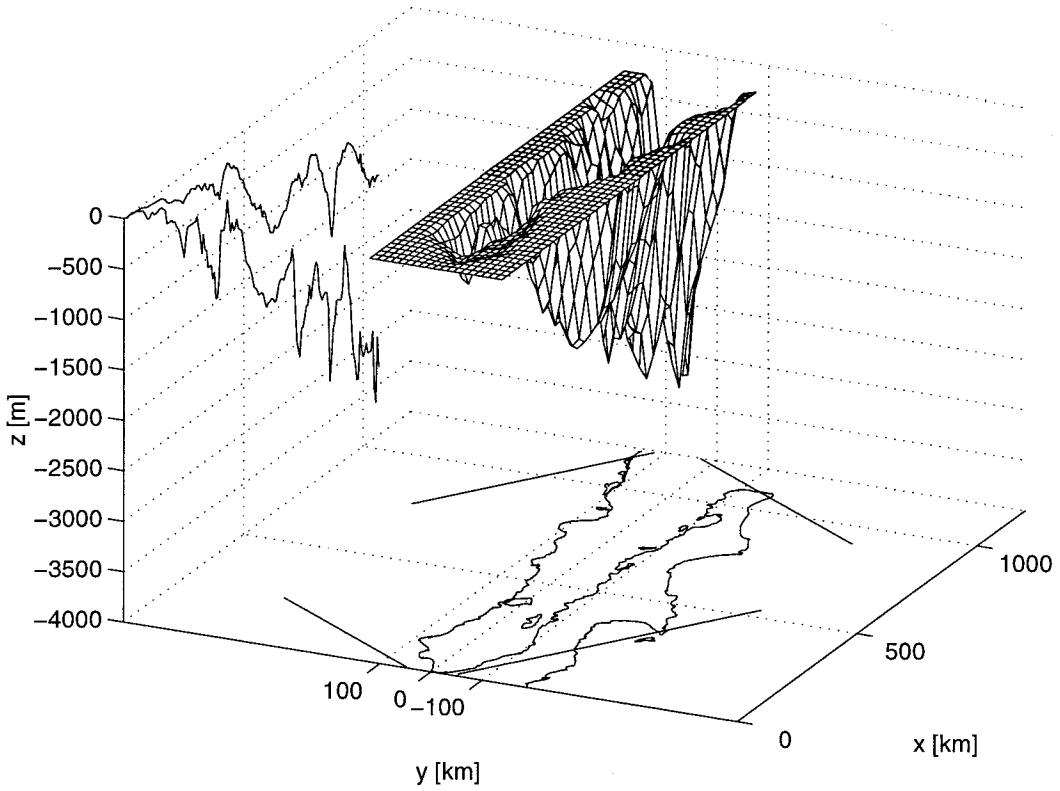

FIG. 1. Geometry of the Gulf of California. In the (x, z) plane are shown the mean and maximum depth as a function of the longitudinal coordinate x. In the horizontal plane, (x, y), are shown the coastline, the 23°N and 32°N parallels, and the 107°W and 115°W meridians.

An estimate of the whole-gulf average of the surface velocity coincided well in phase and was smaller in magnitude than the result of RM89 for the Guaymas Basin. The correlation of this velocity with the seasonal variation of the subsurface pressure was strongly indicative of a baroclinic structure. The corresponding value of the long gravity wave speed, also known as ''separation constant,'' was found to be equal to $c = 1.6 \pm 0.1$ m s^{-1}, from the analysis of the annual signal, or to $c = 1.6 \pm 0.3$ m s^{-1}, from the semiannual one. Finally, an extremely simple model suggested that the changes in sea level were mainly due to the forcing at the mouth, by the Pacific Ocean, with direct wind forcing being only responsible for the along-gulf slope.

Finally, CLR94 calculated the heat content $\mathcal{H}$ down to 400 m (or the bottom, if shallower) and the heat flux through the surface Q, as a function of the along-gulf coordinate x (and integrated in the across-gulf direction). The (vertically integrated) horizontal heat flux $\mathcal{F}^x$ was then estimated by calculating its divergence $\partial\mathcal{F}^x/\partial x$ from the heat balance equation

$$\frac{\partial\overline{\mathcal{H}}}{\partial t} + \frac{\partial\overline{\mathcal{F}^x}}{\partial x} = \overline{Q} \qquad (1)$$

and then integrating in x from the head (where $\overline{\mathcal{F}^x} = 0$). All throughout this paper an overbar denotes an across-gulf, that is, y-, average. The results fully confirm those of RM89 in the sense of the fundamental importance of horizontal heat transport: On an annual average, 18 PW (1 PW = 10^{12} W) enter through the surface and exit to through the mouth, but the seasonal variation is more important. At the annual frequency, the heat import/export through the mouth equals 40 PW and is maximum around 18 May, whereas the heat entering/exiting through the surface equals 20 PW and has its maximum about 10 June. As a consequence, the annual heating of the Gulf of California equals 59 PW and is maximum around 26 May. This is shown in Fig. 2, where the solid curve represents the seasonal heating, sum of the heat input through the surface (dashed curve) plus that entering through the mouth (dot–dashed curve). It is clear that the second one, the horizontal heat flux, is quite important; the purpose of this paper is to shed some light on the physical origin of this process.

Half a century ago, Pattullo et al. (1955) made an analysis of worldwide data showing that recorded sea level is high in the summer/fall and low in the winter/spring, and furthermore coincides very well with the steric level due to the seasonal heating and cooling of the upper 100 m or so (i.e., isostatic conditions). Roden (1964) noted a similar result for the Gulf of California

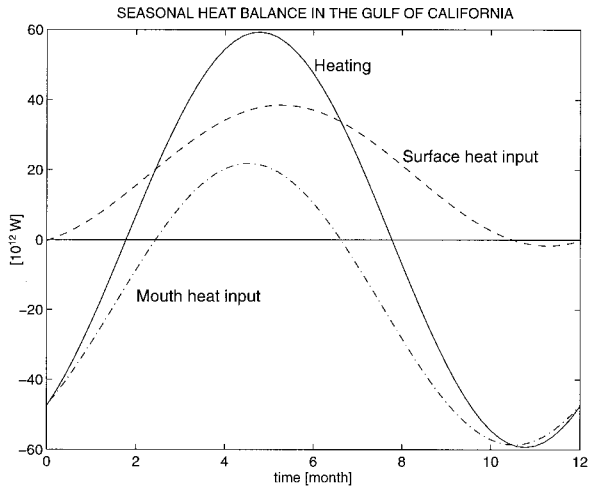

FIG. 2. Global heat balance for the Gulf of California (average plus annual harmonic). The heating (solid curve) is produced by the heat input through the surface (dashed) and through the mouth (dot–dashed).

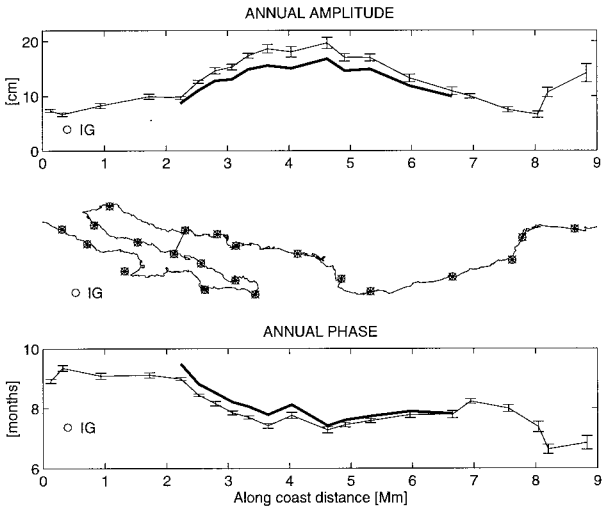

FIG. 3. Amplitude (top) and phase (bottom) of the annual harmonic of sea level on the Pacific coast of Mexico; the locations of the tidal stations are indicated in the middle graph. **IG** represents data from Guadalupe Island, some 270 km from the coast. The thick solid line joins the amplitudes and phases of the subsurface pressure, that is, surface elevation corrected with atmospheric pressure, along the Gulf of California coastline.

and RM89 did likewise for the Guaymas Basin including the geostrophic slope. Figures 3 and 4 show the amplitude and phase of the annual and semiannual harmonics of sea level in the Pacific coast of Mexico. Subsurface pressure (i.e., sea level corrected with atmospheric pressure) is shown with a heavy line for the stations of the Gulf of California; this correction is small but not insignificant. In the large scale it can be seen in both cases a phase propagation toward the pole, corresponding to a phase speed of a few meters per second. However, in the Gulfs of California and Tehuantepec the phase signals are not so clear, and there is a marked increase in the amplitude for both harmonics. Guadalupe Island, some 270 km from the Baja California peninsula, has a seasonal signal quite distinct from that of nearby coastal stations; this is unlike the case of Cedros Island (third station from the left), which is 40 km from the coast. This is evidence of a coastally trapped phenomenon, probably in the form of free and wind-forced baroclinic Kelvin waves, modified by the bottom topography and coast curvature.

The coincidence of recorded and steric levels, pointed out by Pattullo et al. (1955), might lead to the idea of a local phenomenon, namely, that the latter is caused by the heat input or output through the sea surface. At least for the Gulf of California, this idea is incorrect since the evidence quoted above points toward an important horizontal heat flux $\overline{\mathcal{F}^x}$. It will be shown here that $\overline{\mathcal{F}^x}$ can indeed be largely associated with an adiabatic process: a baroclinic wave excited at the mouth of the gulf by the global sea level variation observed by Pattullo et al. and partly shown in Figs. 3 and 4. It will also be proposed that this signal propagates essentially as a coastally trapped Kelvin wave. In a sense, the dynamics at the annual frequency have a similarity with the semidiurnal tide (Hendershott and Speranza 1971): both are co-oscillations with the Pacific Ocean because the direct forcing is not as important (although this is much more so in the case of the tides). There is, however, an important difference: For the barotropic tide the gulf is much narrower than the deformation radius, whereas the baroclinic deformation radii are smaller than the width of the gulf. Thus, in the first case it is not surprising that a one-dimensional model can represent correctly the tide (Ripa and Velázquez 1993), but one does not expect this a priori for baroclinic motions because in a transversely integrated model the Coriolis

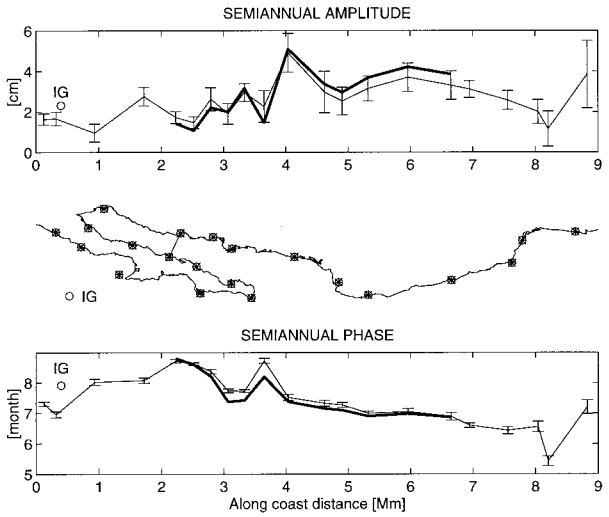

FIG. 4. As in Fig. 3 but for the semiannual component. Notice the distinct characteristic of the Guadalupe Island data.

force disappears from the prognostic equations (it appears only to diagnose the transversal pressure gradient). However, the Kelvin wave scenario allows one to explain why a one-dimensional model (as used in R90) can provide a good representation of the *transversely averaged* fields. It is interesting to note that Kelvin-like signals have also been used to explain mesoscale variability in the Gulf of California (Merrifield and Winant 1989; Merrifield 1992; Gjevik and Merrifield 1993). Beier (1997) has performed a horizontally bidimensional modeling of the Gulf of California, which confirms and enriches the Kelvin wave scenario conjectured here.

This paper has two main goals: First, to show that at the annual frequency, the horizontal heat transport estimated by CLR94 is mainly due to the horizontal temperature advection produced by a baroclinic velocity field. Second, to use a very simple model, linear and across-gulf integrated but including the effects of an irregular bathymetry and coastline, to determine the relative importance of the forcing by the Pacific Ocean, by the wind, and by heat flux through the surface.

2. Data analysis

The starting point is observations of temperature and salinity

$$T(x_i,y_i,z_i,t_i),\ S(x_i,y_i,z_i,t_i),$$

(selected from CICESE's ''historical'' databank) where (x,y) are (along, across) gulf Cartesian coordinates,[1] $-z$ is depth, and t is time. In addition, monthly means of sea level

$$\eta(x_\alpha,y_\alpha,t)$$

and atmospheric pressure are also used, where (x_α,y_α) denotes the positions of the network of tidal stations on both coasts of the Gulf of California (see Figs. 3 and 4).

These data are reduced in two different ways: First, the T and S at a given (x,z,t) are least squares fitted to a straight line in y; that is,

$$T \sim \overline{T}(x,z,t) + \overline{T}_y(x,z,t)(y - \overline{y}). \qquad (2)$$

Second, some time series are least squares fitted to an annual harmonic

$$A(t) \sim A_0 + A_1 \cos\omega t + A_2 \sin\omega t, \qquad (3)$$

where $2\pi/\omega = 1$ yr, and A may represent η at a certain (x,y), $\overline{T}$, $\overline{T}_y$, $\overline{S}$, or $\overline{S}_y$ at a certain (x,z), or some of the variables defined below.[2] The Gulf of California has an important hydrographic variability in across-gulf scales smaller than its width as well as in timescales smaller than a year (Robles and Marinone 1987); these ''mesoscale'' signals conspire against the significance of fits (2) and (3), respectively. Consequently, a set of bins along the gulf were defined and the observations included in each bin were considered to be representative for the central x of that bin. For reasons that will become clear in section 2b, only certain stations were selected in each bin, according to the following criteria:

1) The observations had to reach a certain depth, $-z_*$.
2) The cruise had to present a transversal coverage good enough for (2) to be significant.
3) The bins had to be long enough so that, with the cruises selected, there was a good enough temporal sampling for (3) to be robust.

Significance of the fit (2) was not checked; it will be argued in section 2b that it corresponds to a signal-to-noise ratio of the order of 1 or even less, and therefore its success is evaluated a posteriori, by the results. Goodness of fit (3) is depicted throughout this paper by ''uncertainty bars'' of one standard deviation (see RM89), which do not include any other source of random errors.

The number of stations per bin/month or year/month is depicted in Fig. 5 and the selected bins are shown in Table 1. The first column shows a label (that identifies the bin and the maximum depth $-z_*$) to be used in subsequent tables. The second column indicates the name of the bin: ''Head'' corresponds to the shallowest part of the gulf, north of the big islands. Ángel is in the region of Ángel de la Guarda Island; only observations east of the island were considered; that is, Ballenas Channel is excluded from this analysis. Tiburón corresponds to the region of the other big island. The Guaymas bin is in the basin with the same name, which is one of the best sampled regions in the gulf; the Guaymas–Santa Rosalía transect studied by R89 belongs to this bin. Finally, Yávaros, Topolobampo, and Mouth are the last three bins, in the deep southern basins (see Fig. 1 or CLR94 for a map of the Gulf of California). The third column in Table 1 shows the extent of each bin, in the form of the minimum and maximum distances to the head. Notice that all the bins are 150 km long and that some of the bins overlap (i.e., have some common data) in order to fulfill the requirements of minimum transversal and temporal coverage. The fourth column shows the maximum depth, $-z_*$; for most bins it was possible to choose two values of this variable in order to compare results. Finally, the last two columns show the number of cruises and the total number of stations

[1] Let (μ,λ) be Mercator coordinates; $\mu = \log[(1+\sin\theta)/\cos\theta]$, where θ is latitude. Then Cartesian coordinates (x,y) are defined by a counterclockwise rotation of $\alpha = 33.52°$, from a center located in $(\theta_0, \lambda_0) = (27°\text{N}, 111°\text{W})$, and such that x increases toward the mouth and y toward the continent. In sum, $(x - x_0) + i(y - y_0) = R\cos\theta_0\,[(\mu - \mu_0) - i(\lambda - \lambda_0)]\exp i(\pi - \alpha)$, where R is the radius of the earth.

[2] Sea level and atmospheric pressure records, which are much more complete than the hydrographic ones, were actually analyzed into the first and second annual harmonic.

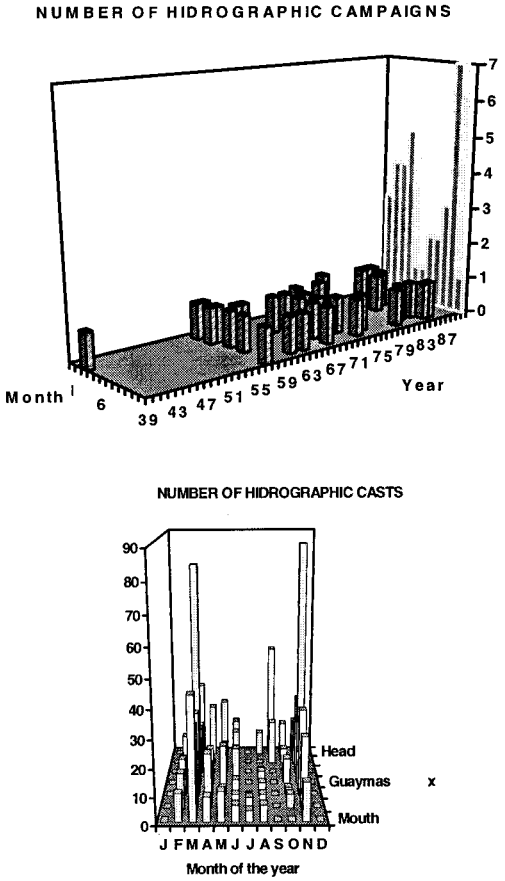

FIG. 5. Hydrographic data availability, classified by month and year (top) and longitudinal bins (bottom).

selected for each bin. (For instance, for the Head bin there are 12 cruises with data down to 70 m, but only 6 cruises with data down to 140 m, and in both cases there on average 13 stations per cruise.)

a. Sea surface elevation and heat content

Sea level is the variable best sampled; its annual analysis (3) is quite robust. As an example, Fig. 6 shows the monthly means (individual points) and annual analysis (curves) at two stations in the middle of the gulf, which practically face each other. The fit at Guaymas, on the continental coast, explains 96% of the variance (corresponding to a random error per point of 3 cm) and predicts a maximum elevation of 20 cm reached on 9 August (± 1 cm and ± 3 d). On the other hand, the fit at Santa Rosalía, on the Baja California coast, explains 98% of the variance (2 cm error per point) and predicts a maximum elevation of 15 cm reached on August 27 (± 0.5 cm and ± 2 d). The differences between both stations are larger than the corresponding uncertainties and are consequently rendered statistically significant: the observed sea surface elevation at the second station has about 22% less amplitude and a lag of 19 d with

TABLE 1. Longitudinal bins.

Label	Section	$x - x_{mouth}$ (km)	$-z^*$ (m)	Number of t	Number of y
He07	Head	70–220	70	12	151
He14			140	6	81
Án20	Ángeles	220–370	200	7	59
Án28			280	5	44
Ti14	Tiburón	350–500	140	9	88
Gu39	Guaymas	500–650	390	19	198
Gu90			900	11	134
Yá49	Yávaros	690–840	490	13	104
Yá53			530	9	74
To48	Topolobampo	820–970	480	14	103
To61			610	10	80
Mo49	Mouth	950–1100	490	13	104

respect to the first station. The distance from Guaymas to Santa Rosalía along the coast is of the order of 1 Mm, and therefore this lag is equivalent to a signal propagating at about 1 m s^{-1} (see also the bottom graphs in Figs. 3 and 4). It is tempting to think of a baroclinic Kelvin wave forced by the Pacific Ocean at the northern part of the mouth and traveling around the gulf while being slightly dissipated by friction. This conjecture is developed in section 3. The difference in the monthly values of sea level between both stations is shown in the bottom panel of Fig. 6, normalized to give a surface velocity through the geostrophic balance

$$\bar{u}_{\text{surf}} = -f^{-1}g\overline{\partial\eta/\partial y}. \tag{4}$$

The solid curve shows again the prediction of the annual analysis (3). Although not as good as that of the indi-

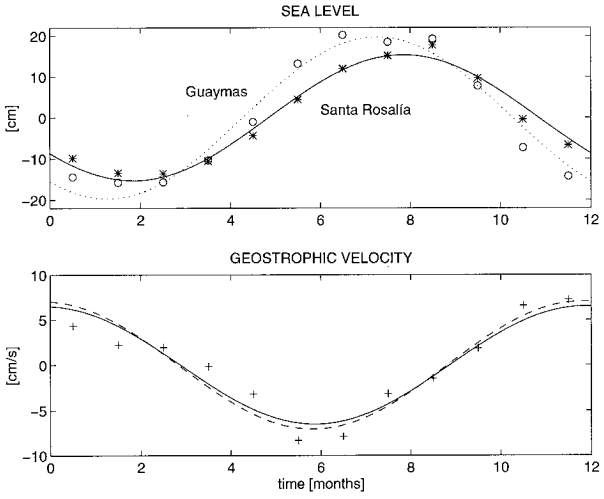

FIG. 6. Monthly mean and annual harmonic of (top panel) sea level at two stations in the mid gulf (this section is indicated by a line in the middle graphs of Figs. 3 and 4) and (bottom panel) surface geostrophic velocity calculated from the slope between both stations (solid line) and corrected with atmospheric pressure (dashed line). Notice that sea level increases when the surface velocity is incoming ($\bar{u} < 0$).

TABLE 2. Sea level and heat content. Uncertainties in this and following tables are one standard deviation, derived from the goodness of the temporal fit.

	$\check{\eta}$		$\overline{\mathcal{H}}$		$\overline{\mathcal{H}}/\check{\eta}$	EV
Label	(cm)	(d)	(10^9 J m^{-2})	(d)	(10^{10} J m^{-3})	(%)
He07	15.2 ± 0.6	30/8 ± 2	1.3 ± .2	19/9 ± 9	0.8	90
He14			2.1 ± .2	26/9 ± 13	1.2	82
Án20	15.2 ± 0.6	29/8 ± 2	1.7 ± .3	31/8 ± 11	1.1	100
Án28			2.1 ± .7	21/8 ± 14	1.4	98
Ti14	15.0 ± 0.6	27/8 ± 2	1.6 ± .5	13/8 ± 15	1.0	92
Gu39	14.6 ± 0.6	24/8 ± 2	2.2 ± .4	20/8 ± 8	1.5	99
Gu90			2.0 ± .5	5/8 ± 8	1.3	88
Yá49	13.1 ± 0.5	2/9 ± 2	2.2 ± .6	26/8 ± 13	1.6	98
Yá53			2.3 ± .6	15/8 ± 15	1.6	90
To48	12.7 ± 0.4	5/9 ± 2	2.1 ± .4	26/8 ± 13	1.7	96
To61			1.6 ± .4	8/8 ± 14	1.1	77
Mo49	11.0 ± 0.4	11/9 ± 2	2.1 ± .5	21/9 ± 14	1.9	97

vidual elevations, this fit is nevertheless significant: 91% of the variance is explained, corresponding to a random error of 1.6 cm s^{-1}. The maximum velocity (toward the mouth) is predicted to be equal to 6.5 ± 0.7 cm s^{-1} and to occur on 28 December ± 6d.

From now on, values of η will be corrected by atmospheric pressure; that is, rather than being true elevation in, say, centimeters, η will denote subsurface pressure in centimeters of water. This correction is small but not insignificant. For instance, the average of both complex amplitudes correspond to a maximum of sea surface elevation, which changes from 17.2 ± 0.6 cm on 17 August ± 2d, before the correction, to 14.6 ± 0.6 cm of water on 24 August (24 ± 2d), after adding the atmospheric pressure. Similarly, the across-gulf averaged surface velocity $\overline{u}_{surf}$ at the Guaymas bin changes from (6.8 ± 1.1) cm s^{-1} on 27 December ± 9d, before the correction, to 7.1 ± 1.1 cm s^{-1} on 26 December ± 9d after adding the atmospheric pressure. For the velocity, the atmospheric pressure correction is smaller than the uncertainty of the annual harmonic fit (see dashed line in Fig. 6).

The second column of Table 2 shows the annual analysis (3) of the mean of surface elevations measured at both coasts $\check{\eta}$, which is taken as representative of the across-gulf average $\overline{\eta}$. (If the signal is trapped to the coasts and approximately in phase, as in the Kelvin wave hypothesis, then the magnitude of $\check{\eta}$ is expected to be larger than that of $\overline{\eta}$.) The amplitude $\sqrt{\check{\eta}_1^2 + \check{\eta}_2^2}$, where the subscripts 1 and 2 are those of (3), varies from 15.2 ± 0.6 cm at the head to 11.0 ± 0.4 cm at the mouth, whereas the phase $\arctan(\check{\eta}_2/\check{\eta}_1)$ shows a maximum elevation ranging from late August at the head through early September in the mouth. The annual analysis (3) of the across-gulf averaged heat content, from the surface down to $-z_*$,

$$\overline{\mathcal{H}}(x, t) := \rho C_p \int_{z^*}^{0} \overline{T}(x, z, t)\, dz,$$

(third column in Table 2) shows a phase very close to that of $\check{\eta}$. Consequently, one might attempt the least squares fit

$$\overline{\mathcal{H}}(x,t) \sim \mu_{\mathcal{H}}\, \check{\eta}(x,t). \tag{5}$$

The last column in Table 2 shows that, indeed, this is quite a good fit, with an ''explained variance'' between 80% and 100% (see appendix A). Not only is the correlation between $\overline{\mathcal{H}}(t)$ and $\check{\eta}(t)$ very good, but in section 2c it will be shown that the value obtained for the proportionality coefficient $\mu_{\mathcal{H}}$ is precisely what is expected for a baroclinic signal. The results of Table 2 are also shown in Fig. 7 along with the heat content calculation of CLR94. Even though the hydrographic database is the same, there are some differences between the results of CLR94 and those of this paper, due to the use of a diverse value of maximum depth as well as the data selection done here in order to get a significant transversal and temporal least squares fit, as explained at the beginning of this section.

b. Longitudinal velocity and heat flux

The transversal density gradient was used to estimate a mouthward velocity profile $\overline{u}(x,z,t)$ by means of

$$f\frac{\partial \overline{u}}{\partial z} = g(\alpha_S \overline{S}_y - \alpha_T \overline{T}_y) \tag{6a}$$

$$\int_{z^*}^{0} \overline{u}\, dz = 0, \tag{6b}$$

where α_S and α_T are the haline contraction and thermal expansion coefficients. This velocity field was in turn used to estimate the advection contribution to the mouthward heat flux (across-gulf averaged and integrated from the surface down to $-z_*$) as

$$\overline{\mathcal{F}^x}(x, t) := \rho C_p \int_{z^*}^{0} \overline{u}(x, z, t)\overline{T}(x, z, t)\, dz. \tag{7}$$

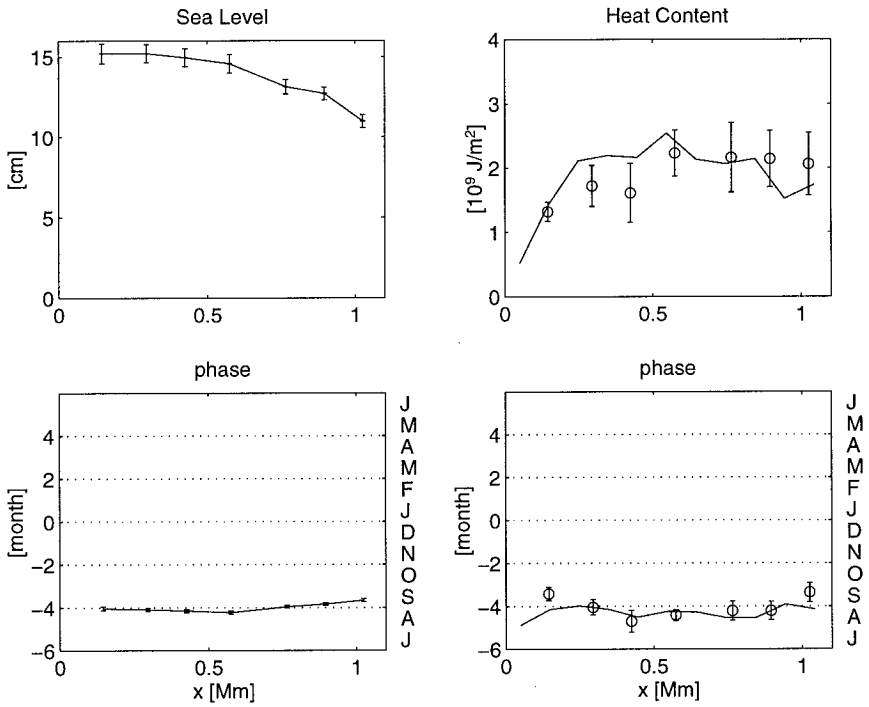

FIG. 7. Amplitudes (top panels) and phases (bottom panels) of variables as a function of the distance x to the head ($x = 1.1$ Mm $= 1100$ km represents the mouth of the gulf). Left: Sea level corrected with atmospheric pressure. Right: Heat content from CLR94 (solid line) and at the various bins from Table 1 (''o'').

The zero-transport condition (6b) used to integrate the thermal wind relation (first equation) guarantees that the heat transport defined here does not depend on the choice of temperature origin. (That condition is equivalent to integrating the thermal wind balance choosing the integration constant so that the kinetic energy is minimum; see RM89.) However, (6b) is quite arbitrary (as most geostrophic calculations are) because the maximum depth $-z_*$ had to be chosen based on the data available for each bin, constrained by the need to have a transversal and temporal coverage good enough to be able to perform the data fits (2) and (3). An alternative to (6b) would be to force $\bar{u}(x, 0, t)$ to be equal to the value calculated from sea surface slope, $\bar{u}_{surf}$ defined in (4). Table 3 compares the results of the annual analysis (3) for both estimates of the surface velocity, that is, calculated as in (4), second column, or in (6), third column; this is also shown at the left panels of Fig. 8. Both estimates of the surface velocity are indeed compatible, with differences within the estimated uncertainties, except for the phases in the (shallow) first two bins and at the mouth.

TABLE 3. Transversely averaged surface velocity.

	$\bar{u}(\eta)$		$\bar{u}(T, S)$	
Label	(cm s^{-1})	(d)	(cm s^{-1})	(d)
He07	1.4 ± 1.1	7/6 ± 46	1.1 ± .6	19/1 ± 23
He14			1.6 ± 1.4	28/2 ± 70
Án20	1.5 ± 1.0	18/12 ± 39	3.6 ± 1.0	13/10 ± 21
Án28			4.3 ± 1.6	3/10 ± 27
Ti14	4.0 ± 1.0	23/12 ± 15	4.1 ± 1.4	8/1 ± 22
Gu39	7.1 ± 1.1	26/12 ± 9	6.5 ± 1.1	2/1 ± 7
Gu90			9.6 ± 3.5	6/1 ± 10
Yá49	5.4 ± 0.7	21/12 ± 7	7.0 ± 2.4	7/1 ± 14
Yá53			8.2 ± 1.8	4/1 ± 11
To48	6.4 ± 0.7	3/1 ± 6	8.7 ± 1.9	24/1 ± 12
To61			11.3 ± 2.0	10/1 ± 8
Mo49	6.1 ± 0.7	10/1 ± 5	8.1 ± 1.7	3/3 ± 14

Even with a much better vertical coverage, the estimate of the across-gulf average of the baroclinic velocity $\bar{u}(x, z, t)$ would still be quite difficult because the transversal fit (2) is not very robust. For instance, RM89 made a similar fit in y, but using a second-order polynomial, which also gives an estimate of the surface vorticity $-\overline{u_y}$; these results show that $\overline{u_y} \times (\frac{1}{2})W$ (where W is the width of the gulf) is typically larger than $\bar{u}$. The *barotropic* velocity has a negligible transversal average (i.e., it can be shown—using mass conservation—to have an annual amplitude of 1.6×10^{-5} m s^{-1} at the mouth), but it might contribute significantly to the current near either coast. For instance, a mass flux of $\pm 7 \times 10^6$ m^3 s^{-1} on either side of the section corresponds to a velocity of 5 cm s^{-1}, similar to the baroclinic signals reported here. (This barotropic current would corre-

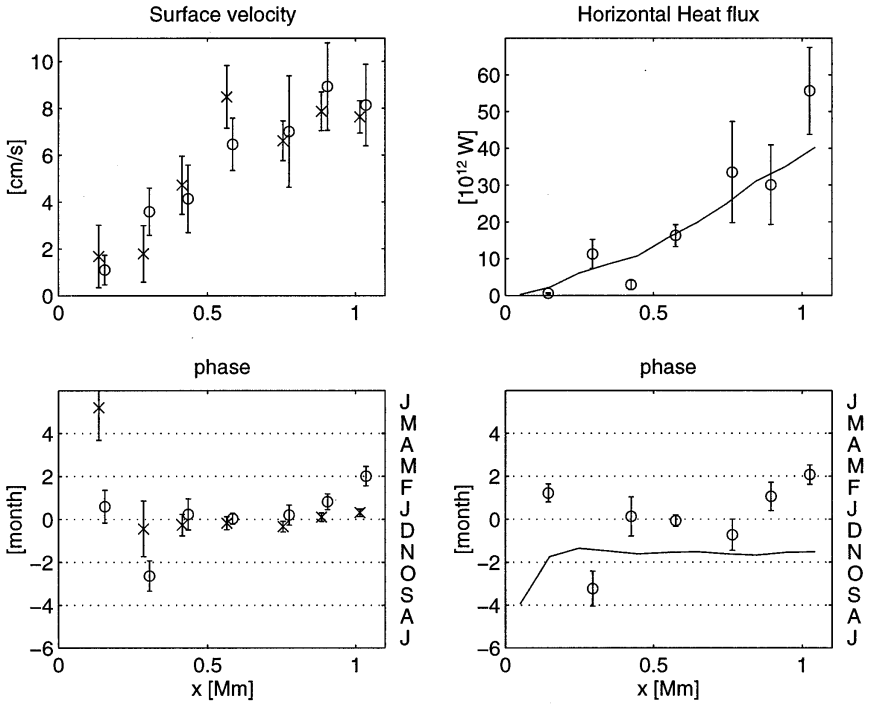

FIG. 8. Left: Geostrophic surface velocity calculated from sea level ("×") or hydrographic data ("o"). Right: Horizontal heat flux, from CLR94 (solid) and evaluated by advection of the geostrophic velocity ("o"). (Display as in Fig. 7.)

spond to a vorticity of about $\pm 0.007f$, whereas RM89 report values as large as $\pm 0.06f$ for the surface baroclinic vorticity). Given the arbitrariness of the value of $-z_*$ (dictated by data availability) the agreement between both calculations of the surface velocity, shown in Table 3 and Fig. 8, is surprisingly good.

The results of the annual analysis (3) of the horizontal heat flux are presented in the right of Fig. 8. The symbols correspond to $\overline{\mathcal{F}^x}$ estimated from the temperature advection (7) by the geostrophic velocity (6), whereas the dashed line represents $\overline{\mathcal{F}^x}$ calculated in CLR94 using the heat balance (1), that is, x-integrating the difference between heating and surface heat flux. It is important to point out that two completely different and independent calculations are being compared in this figure. Although the phases (lower panel in Fig. 8) are different, the agreement between the amplitudes (top panel) is surprisingly good. Figure 8 can be taken as strong evidence that horizontal heat flux at the annual frequency (which Fig. 2 showed to be a very important component of the seasonal heat balance) is mainly produced by advection, as in (7). Not surprisingly, surface velocity and the horizontal heat flux are strongly correlated, as indicated in Table 4, where the fit

$$\overline{\mathcal{F}^x}(x,t) \sim \mu_{\mathcal{F}}\, \bar{u}(x,z=0,t) \qquad (8)$$

is shown to be significant (blank entries in the last column correspond to a negative value of $\mu_{\mathcal{F}}$ or to an explained variance smaller than 50%). Moreover, in section 2c it will be argued that the value of the proportionality constant $\mu_{\mathcal{F}}$ is what is expected for a dominance of the gravest baroclinic mode, which coincides with the results of R90. This proportionality was expected from the following two results presented in RM89. 1) The along-gulf current varies nearly in phase (or counterphase) at different depths. 2) The temporal variation of the product uT is dominated by that of the current; that is, $\delta(uT) \sim \langle T\rangle\, \delta u \gg \langle u\rangle\, \delta T$, where δ denotes seasonal variation and $\langle\cdots\rangle$ temporal mean.

TABLE 4. Longitudinal heat flux.

	$\overline{\mathcal{F}}^x\,\Delta y$		$\overline{\mathcal{F}}^x/\bar{u}(T,S)$		$\overline{\mathcal{F}}^x/\bar{u}(\eta)$	
Label	(10^{12}W)	(d)	(10^9 J m^{-2})	(%)	(10^9 J m^{-2})	(%)
He07	0.6 ± .2	7/2 ± 13	0.4	90	—	—
He14	3.2 ± .3	31/3 ± 12	1.3	73	—	—
Án20	11 ± 3	25/9 ± 25	2.0	90	—	—
Án28	24 ± 7	24/9 ± 26	3.7	97	—	—
Ti14	3 ± 1.3	1/1 ± 27	0.5	98	0.5	96
Gu39	16 ± 3	30/12 ± 8	1.7	100	1.5	100
Gu90	49 ± 28	8/1 ± 16	3.3	100	4.4	96
Yá49	34 ± 14	10/12 ± 22	2.2	79	3.1	96
Yá53	40 ± 7	17/12 ± 10	2.4	92	3.7	99
To48	29 ± 11	31/1 ± 21	1.8	99	2.2	77
To61	51 ± 15	14/1 ± 13	2.4	99	4.2	96
Mo49	56 ± 12	5/3 ± 14	2.8	100	—	—

However, not everything goes well with this independent calculation of the horizontal heat flux: The temporal fit (3) not only provides a value of the annual component of $\overline{\mathcal{F}^x}(x,t)$, but also gives an estimate of its temporal average $\langle\overline{\mathcal{F}^x}(x)\rangle$, which is in complete disagreement with those calculated by CLR94. The estimates of $\langle\overline{\mathcal{F}^x}(x)\rangle$ obtained here are an order of magnitude smaller and with ''random'' signs. In other words, and unlike the case of the annual harmonic, the annual mean of the horizontal heat flux calculated from advection (7) with the present dataset is at the noise level and cannot explain the more direct observations. The physical mechanism for the annual mean horizontal heat transport in the Gulf of California remains unknown. Finally, horizontal salt flux was also evaluated but it did not present a simple annual time dependence, in agreement with the results of RM89 for the Guaymas Basin. The seasonal freshwater balance in the Gulf of California goes beyond the goals of the present analysis.

c. A physical explanation

The main results of the previous section show that, at the annual frequency, heat content and surface elevation are very well correlated and horizontal heat flux is mainly due to advection and is correlated with the surface velocity. Something that is not always well appreciated is that the water rearrangement produced by a baroclinic wave may produce a considerable change in the local heat content. In fact, it will be shown next that this reversible process explains a large fraction of the seasonal heat variability in the Gulf of California.

Consider for simplicity a model with two homogenous layers (more complicated structures are considered in appendix B). If η and ζ are the sea surface elevation and the vertical displacement of the interface between both layers, then their instantaneous thicknesses are

$$h_1(\mathbf{x}, t) = H_1 + \eta(\mathbf{x}, t) - \zeta(\mathbf{x}, t),$$
$$h_2(\mathbf{x}, t) = H_2(\mathbf{x}) + \zeta(\mathbf{x}, t). \quad (9)$$

Assuming that density is controlled by temperature, the kinematic pressure in each layer is given by the hydrostatic expressions

$$p_1(\mathbf{x}, t) = g\eta(\mathbf{x}, t),$$
$$p_2(\mathbf{x}, t) = g\eta(\mathbf{x}, t) + g\alpha_T(T_1 - T_2)\zeta(\mathbf{x}, t). \quad (10)$$

Now, for baroclinic motions $\eta \ll \zeta$ and the local (change of) heat content is given by

$$\mathcal{H}(\mathbf{x}, t) = -\rho C_p(T_1 - T_2)\zeta(\mathbf{x}, t). \quad (11)$$

Since the net mass transport vanishes for a baroclinic signal, $H_1u_1 + H_2u_2 \approx 0$, then $H_1p_1 + H_2p_2 \approx 0$, which implies $(H_1 + H_2)\eta + \alpha_T(T_1 - T_2)H_2\zeta \approx 0$. With (11) one finally obtains

$$\mathcal{H}(\mathbf{x}, t) \approx \frac{\rho C_p}{\alpha_T}\frac{H_1 + H_2}{H_2}\eta(\mathbf{x}, t), \quad (12)$$

which is of the form of the empirical fit (5). [A value of $\mu_{\mathcal{H}} = \rho C_p/\alpha_T$ in (5) corresponds to the isostatic conditions found by Pattullo et al. (1955) for the world oceans.] For $\rho = 1027$ kg m^{-3}, $C_p = 3985$ J kg^{-1} K^{-1}, and $\alpha_T = 2.1 \times 10^{-4}$ K^{-1}, $\rho C_p/\alpha_T = 1.9 \times 10^{10}$ J m^{-3} is obtained, which is close to the values of $\mu_{\mathcal{H}}$ presented in Table 2, calculated from the least squares fit (5). To be more precise, the values in Table 2 are smaller than the theoretical prediction in (12). This is consistent with the Kelvin wave hypothesis because it yields $|\check{\eta}| > |\bar{\eta}|$.

Moreover, from the (linearized) volume conservation equations

$$\frac{\partial h_j}{\partial t} + \nabla\cdot(H_j\mathbf{u}_j) = 0 \qquad (j = 1, 2), \quad (13)$$

imply for baroclinic motions, such that (12) is fulfilled, the heat balance equation $\partial\overline{\mathcal{H}}/\partial t + \nabla\cdot\mathbf{F}_H = 0$, with $\mathbf{F}_H = \rho C_p(T_1 - T_2)H_1\mathbf{u}_1$; that is,

$$\mathbf{F}_H \approx \frac{\rho C_p c^2}{g\alpha_T}\frac{H_1 + H_2}{H_2}\mathbf{u}_1(\mathbf{x}, t), \quad (14)$$

where

$$c^2 = g\alpha_T(T_1 - T_2)\frac{H_1H_2}{H_1 + H_2}. \quad (15)$$

Relationship (14) is of the form (8); for $c = 1.6$ m s^{-1} (see R90) it is $\rho C_p c^2/g\alpha_T = 2 \times 10^9$ J m^{-2}, which also coincides with the estimated values of $\mu_{\mathcal{F}}$ from Table 4.

Appendix B shows that these relationships are not peculiar to the two-layer model but hold for a more general vertical stratification. Relationships like (12) and (14) are valid for the contribution of each baroclinic mode, as long as (potential) density changes are controlled by temperature. The coefficient $\mu_{\mathcal{H}}$ for (5) is approximately given by $\rho C_p/\alpha_T$; that is, it is independent of the (baroclinic) mode number. On the other hand, the coefficient $\mu_{\mathcal{F}}$ for (8) is given approximately by $\rho C_p c^2/g\alpha_T$, which has a bias toward the gravest baroclinic modes, on account of the factor c^2. Of course, this parameterization of the heat content and horizontal flux is likely to hold at timescales other than the annual one, and therefore these results may have important applications in the monitoring of the thermodynamics of the Gulf of California. I will next argue that most of the observed variability (reported in the section 2) is forced by the Pacific Ocean, at the mouth of the gulf.

3. One-dimensional model

In R90 I suggested that the *across-gulf averaged* seasonal variability in the Gulf of California has the form of a ''standing gravity wave'' in the first baroclinic mode forced at the open boundary, whereas the wind is responsible for the small longitudinal slope of sea level. One may wonder on the validity of this scenario since (unlike the case of the barotropic tide) the baroclinic deformation radius is smaller than the gulf's width. In

order to test it, consider a basin with the shape of a *uniform* box with dimensions similar to those of the Gulf of California.

In the first place, Fig. 9 shows the structure of baroclinic response to a forcing in the mouth with the structure of an incoming Kelvin wave, solution of the system (C1) in appendix C, with $F^x = F^y = 0$. This solution is essentially a damped Kelvin wave that goes around the whole rigid boundary: the (equivalent of the) ''continental'' coast, the head, and the ''Baja California'' coast. Appendix C and the graphs on the right of this figure show that the across-gulf average of the fields coincides with the results of the one-dimensional model, except near the head; the turning of the Kelvin wave cannot be simulated by the one-dimensional model.

In the second place, Fig. 10 shows the structure of the solution forced by a uniform wind. When the wind blows toward the head, it forces two waves: 1) a downwelling Kelvin wave in the continental coast, which grows from zero amplitude away from the mouth and then propagates freely around the head and along the Baja California coast (suffering a slight friction damping), and 2) an upwelling Kelvin wave in the latter coast, which grows from zero amplitude away from the head. The superposition of both waves on the Baja California coast gives a signal that decreases toward the mouth. However, if friction is important enough to dampen the downwelling Kelvin wave, near the mouth one can appreciate the growth of the forced upwelling wave. Notice that in addition to this forced/free Kelvin solution, whose across-gulf average is captured by the one-dimensional model, there is a very weak Ekman drift in the interior. Six months later, when the wind blows toward the mouth, the sign of the response is obviously the opposite but its magnitude is the same.

The relationship between a one-dimensional model and the Kelvin wave structure, proved in appendix C and Figs. 9 and 10, is no longer rigorous under the presence of topography and/or a nonuniform friction. Consequently, the Kelvin wave scenario has to be taken as a conjecture, to be proved with a more complete model. The suggestion in R90 is extended next, including the effects of bottom topography as well as wind and thermal forcing at the surface but using, as a first-order model, one with variables transversely averaged. Beier (1997) presents the results of a more complete model, with variation along both horizontal directions.

A one-dimensional two-layer model for the Gulf of California is set up by Eq. (13), written in across-gulf averaged variables,[3] and the momentum equations

$$\frac{\partial \overline{u}_j}{\partial t} + \frac{\partial \overline{p}_j}{\partial x} = F_j,$$

where Eqs. (9) and (10) relate the layer thicknesses and pressures to the surface and interface elevations $\overline{\eta}(x, t)$ and $\overline{\zeta}(x, t)$. The transversal velocity is neglected in the across-gulf averaged equations; that is, it is assumed

$$f\overline{u}_j + \overline{\partial_y p_j} = 0. \tag{16}$$

a. Forcing by the Pacific Ocean

In a first integration of the model, there is no external forcing in the upper layer while the lower layer suffers the action of a bottom drag; that is,

$$F_1 = 0,\ F_2 = -r\overline{u}_2. \tag{17}$$

The parameters of the model were chosen as $H_1 = 70$ m, $T_1 - T_2 = 20$ K, and $r = 2 \times 10^{-5}$ s^{-1}. These values are only considered ''typical;'' no attempt whatsoever was made to optimize them in order to improve the likeness of the model and the observations.[4] Use of the depth-dependent friction coefficient that gives the best fit to the M_2 tide observations (Zavala 1993), $r = (1.8 \times 10^{-3}$ m s$^{-1})/H(x)$, gives results very similar to those corresponding to $r = 2 \times 10^{-5}$ s^{-1}; the latter was adopted for simplicity. Note that in the shallow region where $H(x) < 70$ m, there is only one layer, with $H_1 = \overline{H}(x)$, and thus $F_1 = -r\overline{u}_1$.

The model is forced at the mouth by a baroclinic signal $\overline{p}_1(L, t) = -\overline{p}_2(L, t) \times [H_2(L)/H_1(L)] = g\overline{\eta}_{\text{mouth}}$, where $g\overline{\eta}_{\text{mouth}}$ is an annual harmonic with an amplitude of 0.65 m^2 s^{-2} and a phase of 8 months (i.e., the forcing is maximum at the beginning of September). This value was chosen in order to get the value of $\overline{\mathcal{F}^x}$ at the mouth estimated by CLR94 (this is the only optimization done for the model of this paper). Notice that $g\overline{\eta}_{\text{mouth}}$ is about 60% of the observed value of $g\breve{\eta}_{\text{mouth}}$ (see Table 2). This is consistent with the Kelvin wave hypothesis: the average sea level at both coasts $\breve{\eta}$ (obtained from observations) is larger in magnitude than the across-gulf average $\overline{\eta}$ (used by the model), owing to this signal being trapped to the coasts (see Fig. 9 and appendix C).

The solid line curves in Figs. 11 and 12 show the along-gulf structure of the annual amplitude and phase of $\overline{\eta}$, $\overline{\mathcal{H}}$, $\overline{u}_1$, and $\overline{\mathcal{F}^x}$, which are compared with the observations denoted by *o*. All model variables show a uniform phase, in good agreement with the observations (except perhaps for u_1 and u_{surf}). The amplitude of $\overline{\eta}$ is quite uniform as predicted by the horizontal-bottom uniform-width solution (C7) for $kL \ll 1$ and smaller than the observed coastal mean $\breve{\eta}$. The amplitude of $\overline{u}_1$ increases away from the point where $H_2 = 0$ but, unlike

[3] The variable width of the gulf is taken into account in the volume conservation equation (13), which is modified to the form $\partial(h_j W_j)/\partial t + \partial(\overline{u}_j W_j)/\partial x = 0$, where $W_j(x)$ is the width of layer *j*.

[4] This value of H_1 was found in R90 from the along-gulf sea level slope and an estimate of the geostrophic wind. The value $T_1 - T_2$ gives $c = 1.6$ m s^{-1}, also from R90, for $H_1 = 70$ m when $H_1 + H_2 = 730$ m (the mean depth of the Gulf of California) in (15). Finally, the value of r is the one that gives the best fit to the M_2 tide (Ripa and Velázquez 1993). None of these choices can be strongly justified.

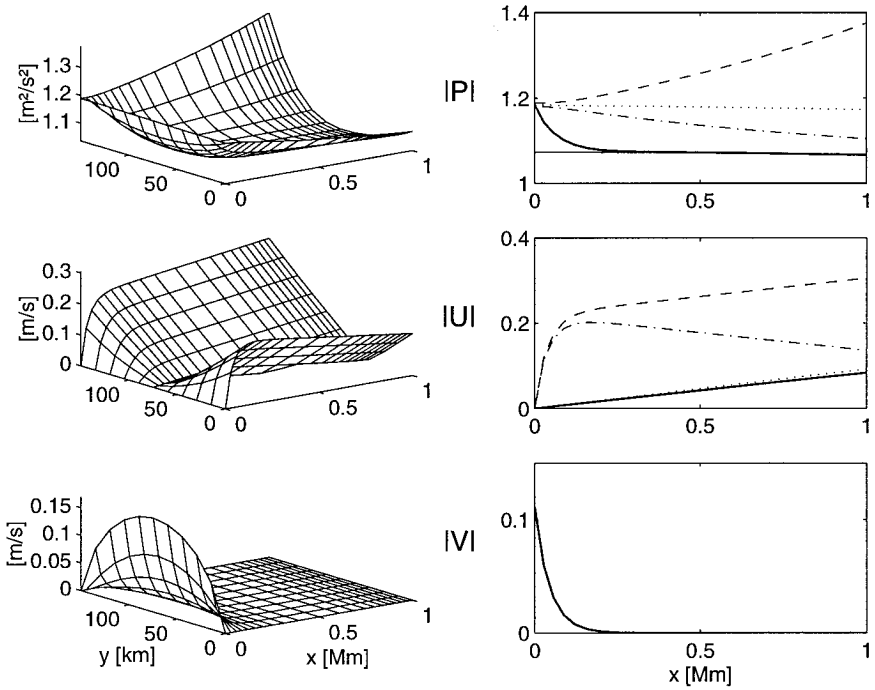

FIG. 9. Amplitude of the annual harmonic of surface pressure (top), longitudinal (middle), and transversal (bottom) velocity. The problem is like that of Taylor, a uniform box, but for a baroclinic vertical mode. The forcing, at the mouth, has the transversal structure of an incoming Kelvin wave. The graphs at the right show the amplitudes at both coasts (dashed and dot–dashed), the amplitude of the average between both coasts (dotted) and the transversal mean (thick solid). The narrow solid curve corresponds to the result of a one-dimensional model (R90), which is a very good approximation of the latter, except near the head.

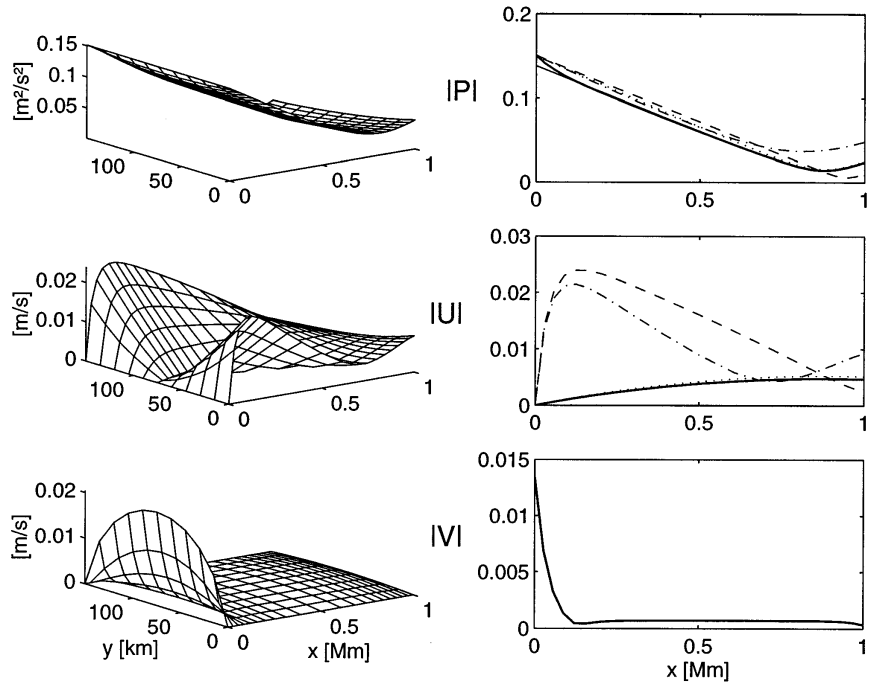

FIG. 10. As in Fig. 9 but for the wind-excited solution. The wind is longitudinal and uniform. The solution is mainly composed of a forced Kelvin wave and a very weak Ekman drift.

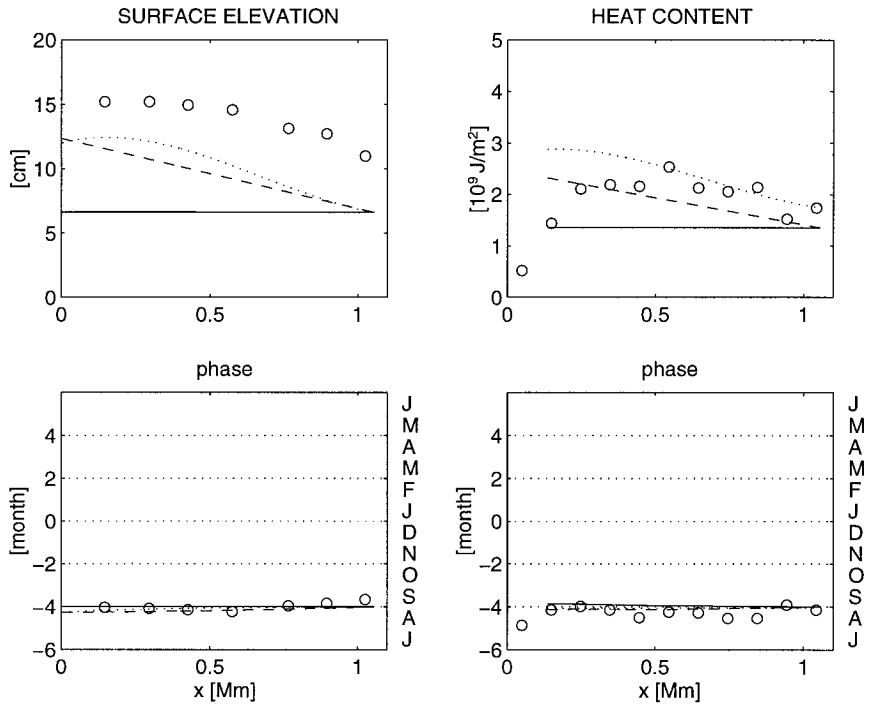

FIG. 11. Comparison of observations (''o'') and predictions of the model with forcing at the mouth (solid), mouth plus wind (dashed), and mouth plus wind plus surface heat flux (dotted). Left: surface elevation (the observations are the mean of both coasts, whereas the model prediction is an across-gulf average). Right: heat content (the observations are those of CLR94). (Display as in Fig. 7.)

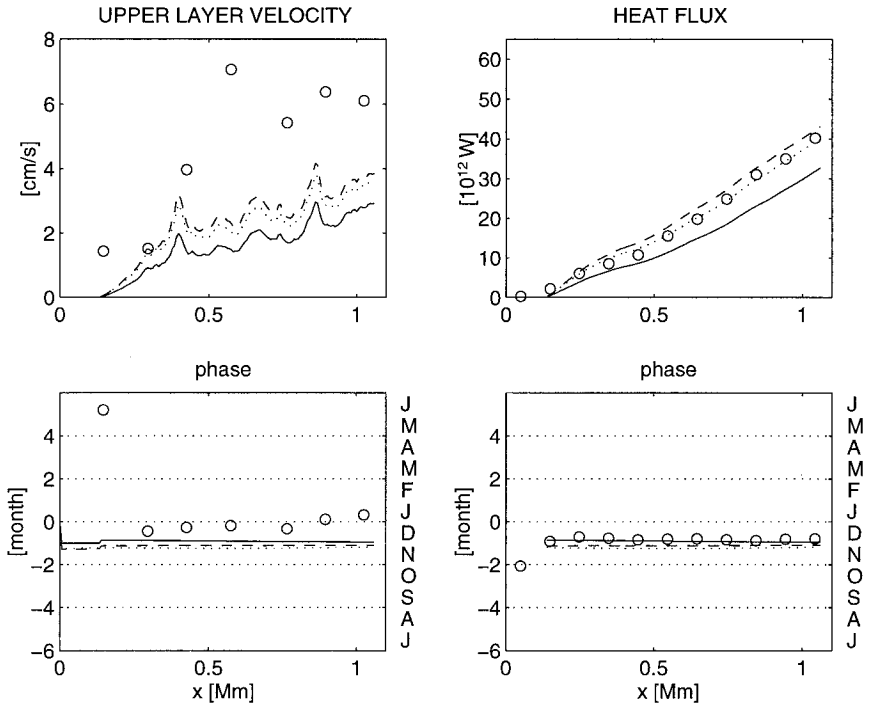

FIG. 12. Left: Estimates of surface velocity from sea surface slope (''o'') vs model predictions for the upper-layer velocity. Right: Horizontal heat flux (the observations are those of CLR94). (Display as in Fig. 11.)

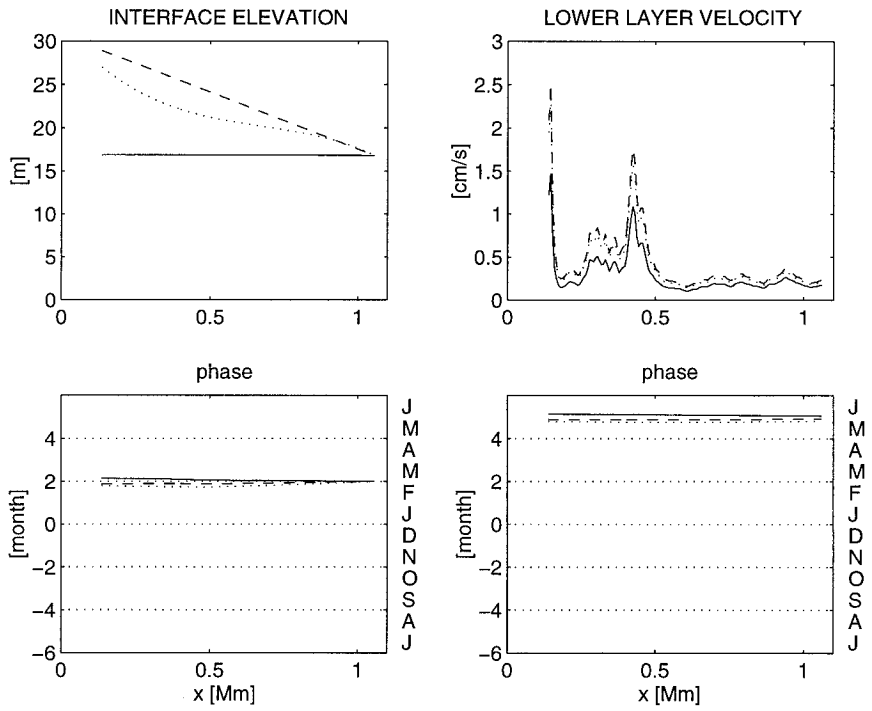

FIG. 13. Model prediction for interface elevation (left) and lower-layer velocity (right). (Display as in Fig. 11.)

the uniform case solution (C7), it reflects the irregularities of the coast (the volume transport $H_1W_1\bar{u}_1$ is a smooth function of x, though). It is not surprising that $|\bar{u}_1|$ is smaller than $|\bar{u}_{surf}|$ because the former represents an average over the upper layer. The agreement between model and observations is also good for $\overline{\mathcal{H}}$ and $\overline{\mathcal{F}^x}$ (certainly within the uncertainty of the observations; see Tables 2 and 4).

Figure 13 shows the model prediction for the interface elevation ζ and the lower-layer velocity $\bar{u}_2$. The velocity structure is baroclinic everywhere; namely, $H_1(x)\bar{u}_1(x) + H_2(x)\bar{u}_2(x) \approx 0$ (notice that $\bar{u}_1$ and $\bar{u}_2$ have a phase difference of π), but the density (or pressure) structure is not: There is a conversion from baroclinic to barotropic potential energy due to the topography. In fact, it was found that $\eta(x)/\zeta(x) \approx -\alpha_T(T_1 - T_2)H_2(L)/H(L)$, that is, the value fixed at the mouth, instead of the being $\eta(x)/\zeta(x) = -\alpha_T(T_1 - T_2)H_2(x)/H(x)$, which is the condition for a purely baroclinic pressure field.

b. Wind forcing

In a second case, wind drag was introduced as a body force in the upper layer. Thus,

$$F_1 = \frac{\tau}{\rho H_1}, \qquad F_2 = -r\bar{u}_2. \tag{18}$$

The value of τ/ρ chosen is that from R90 (amplitude of 3.8×10^{-5} m^2 s^{-2} and phase corresponding to a maximum on 13 February), which comes exclusively from the geostrophic wind calculated from the difference of atmospheric pressure, at sea level, between Guaymas and Santa Rosalia. (There are direct observations of wind in the Gulf of California, but either they come from coastal stations, which are not too representative of the open ocean wind, or the records are too short to calculate the annual component.) The model results including the effects of wind forcing are shown with dashed lines in Figs. 11 and 13. As predicted in R90, the wind only affects the slope of subsurface pressure, through the approximate balance $g\partial\eta/\partial x \approx \tau/(\rho H_1)$, bringing the amplitude of η more in agreement with the observations (see upper left panel in Fig. 11). The effect of the wind on the upper-layer velocity (and consequently, on the horizontal heat flux) is small.

c. Surface heat flux

A process that was not included in the analysis of R90 is the heat input $\bar{Q}$ through the surface of the ocean. Even though it is smaller than that through the mouth, it is so by only a factor of 2 (see Fig. 2), and therefore it is important to inquire about its effect on the annual heat balance. The simplest way to include this process is by allowing for the local heating and cooling of the upper layer, but keeping both the velocity $\bar{u}_1(x, t)$ and the temperature, say $T_1 + T_1'(x, t)$, as depth independent. The latter then changes according to

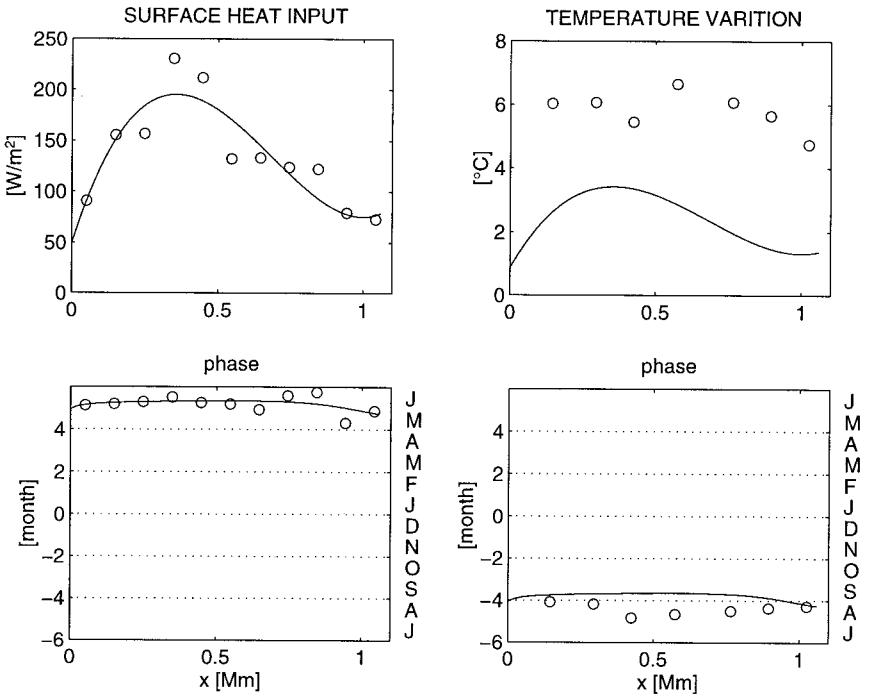

FIG. 14. Left: Heat input through the surface from CLR94 (''o'') and polynomial fit (line). Right: Temperature change, surface observations (''o''), and model prediction for the upper layer (solid line). (Display as in Fig. 11.)

$$\rho C_p H_1 \frac{\partial \overline{T}_1'}{\partial t} = \overline{Q}_1(x) \cos\omega t + \overline{Q}_2(x) \sin\omega t.$$

(Notice that in these linearized equations the nonlinear term $\bar{u}\partial_x T_1'$ is not included.) Figure 14 shows the annual component of $\overline{Q}(x,t)$, from CLR94, and the corresponding temperature change in the upper layer (the buoyancy variation is of the order of 10%). The amplitude of the model temperature in the upper layer $|T_1'|$ is smaller than the observed *surface* signal $|T_{surf}'|$. In a more realistic model one expects the heat entering through the surface to be distributed nonuniformly in the upper layer (Ripa 1995), putting the model closer to the observations. It is interesting to see that if one raises T_1' to coincide with the surface observations in the deepest half (large x), then the model still underpredicts the T_{surf}' in the shallowest parts. This is consistent with the intense tidal mixing found in this part of the gulf (Paden et al. 1991, 1993).

The temperature inhomogeneity in the upper layer produces a depth-dependent pressure gradient; vertically averaging this force in each layer corresponds to changing from (18) to (see, for instance, Ripa 1993)

$$F_1 = \frac{\tau}{\rho H_1} + \frac{1}{2} H_1 g \alpha_T \frac{\partial \overline{T}_1'}{\partial x},$$

$$F_2 = -r\bar{u}_2 + H_1 g \alpha_T \frac{\partial \overline{T}_1'}{\partial x}. \qquad (19)$$

The solutions corresponding to this forcing are shown with dotted lines in Figs. 11 and 12. At this low frequency, the momentum balance in the upper layer gives the along-gulf sea surface slope by $g\partial\eta/\partial x \approx F_1$. The effect of surface heat flux is similar to that of the wind, but with the opposite sign; for instance, the magnitude of the horizontal heat flux at the mouth is equal to 33 PW, 43 PW, and 40 PW for the forcing (17), (18), and (19), respectively. Thus, of the 20 PW entering and exiting through the surface, only 3 PW go through the mouth on account of the heat flux-induced velocity.

4. Discussion

The annual component of the horizontal heat flux $\overline{\mathcal{F}^x}$ in the Gulf of California is maximum (toward the mouth) in November and has an amplitude that increases monotically from 0 at the head to about 40 PW (1 PW $= 10^{12}$ W) at the mouth (see Fig. 2). This is larger, by a factor of 2, than the corresponding component of the surface heat flux. Here it is shown that, at the annual frequency, $\overline{\mathcal{F}^x}$ is mainly produced by horizontal heat advection produced by a baroclinic velocity signal, and hence is approximately proportional to the surface velocity u_{surf} (see Fig. 8). At the same time, the local heat content $\overline{\mathcal{H}}$ was also found to be proportional to the sea surface elevation η (see Fig. 7). Since u_{surf} can be calculated from the transverse slope of η (see Fig. 6), sea level observations along the coasts of the Gulf of Cal-

ifornia might be very useful to monitor the gross dynamic and thermodynamic state of this basin. A simple (transversely integrated) two-layer model shows that this baroclinic wave is mainly forced by the Pacific Ocean (at the mouth), whereas the wind drag and surface heat flux have a smaller effect on the velocity field (see Figs. 11 and 12). (Their more noticeable effect is an along-gulf slope of the sea surface.) It is conjectured that the boundary-forced signal propagates in the form of an internal Kelvin wave (see Fig. 9) distorted by the topography (see Fig. 1). It is conceivable that in the future an operational model of the Gulf of California will need only hydrographic input at the mouth and sea-surface elevation along the coast.

In sum, the results of this model show that the forcings by the Pacific Ocean, the wind drag, and surface heat flux are responsible for

1) ± 6.6 cm, ± 2.9 cm, and ± 0.9 cm of average surface elevation in the whole gulf (see Fig. 11), where the upper (lower) sign roughly corresponds to fall (spring);
2) $\pm 1.4 \times 10^9$ J m^{-2}, $\pm 0.5 \times 10^9$ J m^{-2}, and $\pm 0.6 \times 10^9$ J m^{-2} of average heat content variability (see Fig. 11), where the upper (lower) sign roughly corresponds to fall (spring);
3) ± 33 PW, ± 10PW, and ∓ 3 PW of heat flux through the mouth (see Fig. 12), where the upper (lower) sign roughly corresponds to winter (summer); and
4) ± 2.9 cm s^{-1}, ± 1.0 cm s^{-1}, and ∓ 0.3 cm s^{-1} of the upper-layer velocity at the mouth (see Fig. 12), where the upper (lower) sign roughly corresponds to winter (summer).

These values clearly demonstrate the dominance of the forcing at the mouth, whose response probably takes the form of a baroclinic Kelvin wave (see appendix C), whereas the wind-forced signal is about a factor 3 smaller. Thus, a great deal of the thermodynamics in the Gulf of California can be explained by an adiabatic process. The results of this paper are corroborated—and modified— by those of a horizontally two-dimensional model with the same linearized dynamics and thermodynamics employed here (Beier 1997).

Nonlinear effects may also be interesting. The interface elevation of the model of this paper has an appreciable amplitude at the place where the thickness of the lower layer vanishes. In a sloping bottom, the vertical displacement of the edge of the interface actually represents an important horizontal excursion (e.g., toward the head when the interface goes up), which is not represented in the linearized model. Inclusion of this phenomenon in a nonlinear model might have interesting consequences on the dynamics and thermodynamics of the upper gulf. Another important point that remains to be studied is the freshwater balance, which has not been analyzed as easily as the heat balance, because salinity has a more complicated seasonal signal than temperature and is also less tied to density.

Acknowledgments. This work has been supported by CICESE's normal funding and by CONACyT (México) under Grant 1282-T9204. The second version of this paper was written while on sabbatical leave at the School of Earth and Ocean Sciences, University of Victoria, British Columbia; financial support from CONACyT (México) and NSERC (Canada) is sincerely appreciated. Gilberto Velázquez and Federico Graef were very helpful with data processing and corrections of the manuscript, respectively.

APPENDIX A

Proportionality of Two Harmonic Signals

Given two harmonic signs $A(t)$ and $B(t)$, consider the hypothesis of their proportionality; that is,

$$A_1\cos\omega t + A_2\sin\omega t \sim \mu\ (B_1\cos\omega t) + B_2\sin\omega t \quad \text{(A1)}$$

for some real μ. Defining $A_1 + iA_2 =: A_M \exp(iA_P)$ and similarly for B, the above relation is written as

$$A_M\cos(\omega t - A_P) \sim \mu\ B_M\cos(\omega t - B_P).$$

Minimizing the time integral of the square of the difference between both sides, one easily obtains

$$\mu = \cos(A_P - B_P)\ A_M/B_M.$$

The ''variance explained'' (VE) is easily seen to be a fraction $\cos^2(A_P - B_P)$ of the original variance; this is largest when both series are almost in phase, $A_P - B_P \approx 0$, or counterphase, $A_P - B_P \approx \pm\pi$, and it is smallest when both series are near quadrature, $A_P - B_P \approx \pm\pi/2$.

In order to determine the ''statistical significance'' of the fit (A1) one needs to compare the value of $A_P - B_p$ with an appropriate random variable with uniform probability distribution. There are two possibilities:

1) the sign of μ is important (e.g., only positive values of μ are physically meaningful, then $A_P - B_P \approx 0$ is good but $A_P - B_P \approx \pm\pi$ is not), or
2) both signs of μ are acceptable.

Let

$$\nu := \min\left|(A_P - B_P)2/\pi \bmod 4\right|;$$

this variable ranges from 0 to 2. The ''confidence level'' (probability of getting by chance a worse result) is then given by

$$\text{1)}\ \text{CL} = \begin{cases} 1 - \nu & \text{if } \nu < 1 \\ 0 & \text{otherwise} \end{cases}$$

in the first case, or

$$\text{2)}\ \text{CL} = |1 - \nu| \text{ in the second one.}$$

A similar analysis for the case when there are two different frequencies involved (e.g., annual and semiannual) can be found in R90.

As an example consider the fits (5) and (8). They

correspond to the first case, because a negative value of μ does not make physical sense. Thus, a 90% confidence level, $\nu = 0.1$, corresponds to $|A_P - B_P| \leq 0.05\pi$ ($\equiv$ 9d, for an annual harmonic) and therefore to a variance explained VE $= 100 \cos^2(A_P - B_P) \geq 97.6\%$. This analysis does not take into account any a priori uncertainty of the phases A_P and B_P.

APPENDIX B

Heat Content and Transport for Baroclinic Modes

Let the horizontal current, (kinematic) pressure, and isopycnal elevation fields be decomposed in vertical normal modes; that is,

$$\begin{aligned} \mathbf{u}(x, y, z, t) &= \sum_j \mathbf{u}_j(x, y, t)G_j'(z) \\ p(x, y, z, t) &= \sum_j p_j(x, y, t)G_j'(z) \\ \zeta(x, y, z, t) &= \sum_j p_j(x, y, t)G_j(z)/c_j^2, \end{aligned} \tag{B1}$$

where the structure functions are the solutions of the eigenvalue problem $c_j^2 G''_j + N^2(z)G_j(z) = 0$, $G_j(-H) = 0$, and $gG_j(0) = c_j^2 G'_j(0)$; for instance, see Ripa 1986. The surface elevation and velocity fields are given by

$$\begin{aligned} \eta(x, y, t) &= \sum_j p_j(x, y, t)G_j'(0)/g =: \sum_j \eta_j(x, y, t), \\ \mathbf{u}_{\text{surf}}(x,y,t) &= \sum_j \mathbf{u}_j(x,y,t)G_j'(0) =: \sum_j \mathbf{u}_j^{\text{surf}}(x,y,t). \end{aligned} \tag{B2}$$

Now, if one assumes that (potential) density is mainly controlled by temperature, then the Brunt–Väisälä profile is given by $N^2(z) = g\alpha_T(dT_{\text{ref}}/dz)$, where $T_{\text{ref}}(z)$is the reference temperature, and the temperature perturbation field is written as $T' = -(dT_{\text{ref}}/dz)\zeta$. Using the expansions (B1) and (B2), it can then be shown that the local heat content is expanded as

$$\mathcal{H} = \rho C_p \int_{-H}^{0} T' \, dz = \sum_j a_j \eta_j(x, y, t), \tag{B3}$$

where $a_j = (\rho C_p/\alpha_T)[1 - G_j'(-H)/G_j'(0)]$. Notice that the barotropic mode does not contribute to $\mathcal{H}$ (namely, $a_0 \approx 0$) as expected. If the surface elevation is dominated by the baroclinic modes, and these are surface intensified, $G_j'(0) \gg G_j'(-H)$, then $\mathcal{H} \approx \mu_{\mathcal{H}}\eta$, with $\mu_{\mathcal{H}} \approx \rho C_p/\alpha_T$. On the other hand, the incompressibility equation for mode j reads $\partial_{pj}/\partial t + c_j^2 \nabla \cdot \mathbf{u}_j = 0$; with (B3) it is $\partial\mathcal{H}/\partial t + \nabla \cdot \mathbf{F}_H = 0$, where $\mathbf{F}_H = \sum_j a_j c_j^2 \mathbf{u}_j^{surf}(x, y, t)$. An alternative derivation is obtained by using the expansions (B1) and (B2) in the definition of $\mathbf{F}_H$, namely,

$$\begin{aligned} \mathbf{F}_H = \rho C_p \int_{-H}^{0} \mathbf{u}T' \, dz = \frac{\rho C_p}{\alpha_T} \sum_j c_j^2 \mathbf{u}_j(x, y, t) \\ \times [G_j'(0) - G_j'(-H)]/g. \end{aligned}$$

Consequently, if *one* baroclinic mode (say, $j = 1$) dominates the surface fields, it then follows that $\mathcal{H} \approx a_1\eta$ and $\mathbf{F}_H \approx a_1 c_1^2 \mathbf{u}_{surf}$, where $a_1 = (\rho C_p/\alpha_T)[1 - G_1'(-H/G_1'(0)] \approx (\rho C_p/\alpha_T)$.

APPENDIX C

Baroclinic Response in a Uniform Box

Consider the evolution of the amplitudes of a single vertical mode (B1) (the subscript j is omitted for simplicity)

$$\frac{\partial p}{\partial t} + c^2\frac{\partial u}{\partial x} + c^2\frac{\partial v}{\partial y} = 0 \tag{C1a}$$

$$\frac{\partial u}{\partial t} - fv + \frac{\partial p}{\partial x} = F^x - \lambda u \tag{C1b}$$

$$\frac{\partial v}{\partial t} + fu + \frac{\partial p}{\partial y} = F^y - \lambda v \tag{C1c}$$

in a uniform channel of length L and width W, say ($0 \leq x \leq L$, $-W/2 \leq y \leq W/2$); $F^x - \lambda u$ and $F^y - \lambda v$ are the longitudinal and transversal components of the sum of wind and bottom drags, projected into that particular vertical mode.[5] Assume that $F^y = 0$ and that the forcing at the mouth ($x = L$) and/or by the wind is harmonic, with frequency ω; for example,

$$F^x = \text{Re}\,(F\, e^{-i\omega t}),$$

where F is uniform. Just like with Taylor's problem (Hendershott and Speranza 1971) it can be shown that the solution to (C1) can be written as the superposition of transversal modes; away from the head the most important ones are both Kelvin waves, one trapped to each coast, which have the form

$$\begin{aligned} p(x, y, t) &= [A^+(x)e^{-\nu y} + A^-(x)e^{\nu y}]e^{-i\omega t} \\ u(x, y, t) &= \nu f^{-1}\,[A^+(x)e^{-\nu y} - A^-(x)e^{\nu y}]e^{-i\omega t} \\ v &= 0, \end{aligned} \tag{C2}$$

where $\nu = (f/c)\sqrt{\omega/(\omega + i\lambda)}$ (the square root is chosen to have a positive real part). The amplitudes of the Kelvin modes satisfy

$$\left(\frac{\mathrm{d}}{\mathrm{d}x} \mp ik\right) A^{\pm}(x) = \gamma F \tag{C3a}$$

$$A^-(L) = B \tag{C3b}$$

$$A^+(0) = A^-(0) \tag{C3c}$$

with

$$\begin{aligned} k &= (\omega + i\lambda)\nu f^{-1} = \sqrt{\omega(\omega + i\lambda)}/c\text{e} \\ \gamma &= (\tfrac{1}{2})\text{sech}(\nu W/2). \end{aligned}$$

[5] For instance, for the baroclinic mode of a two-layer model it is $F^{x,y} = (\tau^{x,y}/\rho H_1)(1 + H_1/H_2)^{-1}$ and $\lambda = r\,(1 + H_2/H_1)^{-1}$.

Notice that (C3a) is solved first for the incoming Kelvin wave [using the value at the mouth $A^-(L)$, which is fixed by the forcing by the deep ocean] and then for the outgoing Kelvin wave [using its amplitude at the head $A^+(0)$, determined by the incoming signal]. This last condition comes from imposing $u(0, y, t) = 0$, which also requires the existence of a set of evanescent Poincaré waves trapped to the head. Figures 9 and 10 show that these Poincaré modes actually produce the turning of the Kelvin wave along the head's coast. In Fig. 10 can also be seen a very weak Ekman drift in the v component (see Beier 1997), which is not represented by the Kelvin part of (C2) of the expansion.

The ratio of the transversal average of the elevation field to the mean of the values of this field in both coasts is given by

$$\frac{\bar{\eta}}{\check{\eta}} = a = \frac{\tanh(\nu W/2)}{\nu W/2}. \tag{C4}$$

Typical parameters for the first baroclinic mode in a box similar to the Gulf of California are $W = 150$ km, $L = 1.1 \times 10^6$ m, $\lambda = rH_1/(H_1 + \overline{H}_2) = 2 \times 10^{-6}$ s^{-1}, $c = 1.6$ m s^{-1}, and $f = 6.8 \times 10^{-5}$ s^{-1} (these are the values used in Figs. 9 and 10). At the annual frequency, $\omega \approx 2 \times 10^{-7}$ s^{-1}, it is $|kL| = 0.43$, $|\nu W| = 2.0$, and $|a| = 0.91$; the corresponding values with no friction are $|kL| = 0.14$, $|\nu W| = W|f|/c = 6.4$, and $|a| = 0.31$. Notice that $kx \ll 1$, and therefore $\cos kx \approx 1$ and $\sin kx \approx kx$ in the solutions discussed below.

Taking the y-average of (C2), and using (C3), the important thing for this paper is to determine to what extent the averaged fields match the solutions of the one-dimensional model equations

$$\frac{\partial \bar{p}}{\partial t} + c^2 \frac{\partial \bar{u}}{\partial x} = 0$$

$$\frac{\partial \bar{u}}{\partial t} + \frac{\partial \bar{p}}{\partial x} = \bar{F} - \lambda \bar{u}, \tag{C5}$$

discussed in R90. This approximation neglects the contribution of $-\overline{fv}$ in the left-hand side of the equation for $\bar{u}$, a term that would have arised in a straightforward across-gulf average of the full equation (C1).

a. Boundary-forced solution

The Kelvin part of the solution of Fig. 9 corresponds to a finite value of $A^-(L)$ and $F = 0$, namely,

$$A^{\pm} = B\, e^{\pm ikx + ikL}, \tag{C6}$$

From (C6) it follows for the solution forced at the mouth: first the geostrophic balance (16) and second

$$\bar{p}(x, t) = M \cos kx e^{ikL - i\omega t}$$

$$\bar{u}(x, t) = i\nu f^{-1} M \sin kx e^{ikL - i\omega t}, \tag{C7}$$

where $M = 2B\overline{\exp[\mp \nu y]} = B \sinh(\nu W/2)/\nu W/2$, which is also the solution of the one-dimensional model (C5) with the boundary conditions[6]

$$\bar{u}(0) = 0$$

$$\bar{p}(L) - (f/\nu)\bar{u}(L) = M.$$

Notice that if $|\nu W|$ is large (the gulf is wider than the deformation radius), then the amplitudes at the coast will be larger than the transversely averaged values for the pressure field, but even more so for the velocity field, because the contribution of both Kelvin waves have equal (opposite) signs for p (u). The Kelvin wave hypothesis predicts an average vorticity

$$-\overline{u}_y(x, t) = \frac{\omega}{\omega + i\lambda} \frac{fM}{c^2} \cos kx e^{-i\omega t}. \tag{C8}$$

(If $\omega \gg \lambda$ then the vorticity is in phase with the pressure and corresponds to the zero potential vorticity, $u_y + fp/c^2 = 0$.) The maximum of $-u_y$ at the surface predicted by this formula is about $0.06 \times f$, which equals the maximum surface values estimated in RM89. This contribution represents a cyclonic (anticyclonic) vorticity in summer–fall (winter–spring) as quoted by Bray (1988), Merrifield and Winant (1989), and Paden et al. (1991).

b. Wind-forced solution

The Kelvin part the solution of Fig. 10 corresponds to solving (C3) with $A^-(L) = 0$ and $F \neq 0$, which yields

$$A^- = -ik^{-1}\gamma F(1 - e^{ikL - ikx})$$

$$A^+ = ik^{-1}\gamma F[(1 - e^{ikx}) - (1 - e^{ikL})e^{ikx}]. \tag{C9}$$

Taking the traversal average of (C2) with these amplitudes, it follows

$$\bar{p} = iak^{-1}F(e^{ikL}\cos kx - e^{ikx})$$

$$\bar{u} = ia\nu f^{-1}k^{-1}F(ie^{ikL}\sin kx + 1 - e^{ikx}), \tag{C10}$$

where a is defined in (C4); this transversely averaged solution corresponds to the boundary condition

$$\bar{p}(L) - \nu^{-1} f \bar{u}(L) = 0$$

at the mouth. Beier (1997) presents an alternative derivation of the wind-forced solution far from the head, which includes the Ekman drift term: neglecting the $(\partial_t + \lambda)v$ term in (C1c) it follows the solution above, but with $\bar{v} = f^{-1}(a - 1)F$ instead of $\bar{v} = 0$.

The one-dimensional model yields solution (C10), but without the factor a. The wind-forced part of $\bar{p}$ is then overestimated by that model, by a factor of a^{-1}; that is, it gives the mean value between both coasts $\check{p}$.

[6] Since v is complex and a function of the frequency, the second boundary condition is usually replaced by $\bar{p}(L) - c\bar{u}(L) = M$, which corresponds to the vanishing friction case.

REFERENCES

Beier, E., 1997: A numerical investigation of the annual variability in the Gulf of California. *J. Phys. Oceanogr.*, **27**, 615–632.

Bray, N., 1988: Thermohaline circulation in the Gulf of California. *J. Geophys. Res.*, **93,** 4993–5020.

Castro, R., M. Lavín, and P. Ripa, 1994: Seasonal heat balance in the Gulf of California. *J. Geophys. Res.*, **99,** 3249–3261.

Gjevik, B., and M. Merrifield, 1993: Shelf-sea response to tropical storms along the west coast of Mexico. *Contin. Shelf Res.*, **13,** 25–47.

Hendershott, M., and A. Speranza, 1971: Co-oscillating tides in long, narrow bays; the Taylor problem revisited. *Deep–Sea Res.*, **18,** 959–980.

Marinone, S., and P. Ripa, 1988: Geostrophic flow in the Guaymas Basin, central Gulf of California. *Contin. Shelf Res.*, **8,** 159–166.

Merrifield, M., 1992: A comparison of long coastal-trapped wave theory with remote-storm-generated wave events in the Gulf of California. *J. Phys. Oceanogr.*, **22,** 5–18.

——, and C. Winant, 1989: Shelf circulation in the Gulf of California: A description of the variability. *J. Geophys. Res.*, **94,** 18 133–18 160.

Paden, C., M. Abbott, and C. Winant, 1991: Tidal and atmospheric forcing of the upper ocean in the Gulf of California. 1: Sea surface temperature variability. *J. Geophys. Res.*, **96,** 18 337–18 359.

——, C. Winant, and M. Abbott, 1993: Tidal and atmospheric forcing of the upper ocean in the Gulf of California. 2: Surface heat flux. *J. Geophys. Res.*, **98,** 20 091–20 103.

Pattullo, J., W. Munk, R. Revelle, and E. Strong, 1955: The seasonal oscillation in sea level. *J. Mar. Res.*, **14,** 88–155.

Ripa, P., 1986: Evaluation of vertical structure functions for the analysis of oceanic data. *J. Phys. Oceanogr.*, **16,** 223–232.

——, 1990: Seasonal circulation in the Gulf of California. *Ann. Geophys.*, **8,** 559–564.

——, 1993: Conservation laws for primitive equations models with inhomogeneous layers. *Geophys. Astrophys. Fluid Dyn.*, **70,** 85–111.

——, 1995: On improving a one-layer ocean model with thermodynamics. *J. Fluid Mech.*, **303,** 169–201.

——, and S. Marinone, 1989: Seasonal variability of temperature, salinity, velocity, vorticity, and sea level in the central Gulf of California, as inferred from historical data. *Quart. J. Roy. Meteor. Soc.*, **115,** 887–914.

——, and G. Velázquez, 1993: Modelo unidimensional de la marea en el Golfo: de California (One dimensional model of the tide in the Gulf of California). *Geofís. Int.*, **32,** 41–56.

Robles, J., and S. Marinone, 1987: Seasonal and interannual thermohaline variability in the Guaymas Basin of the Gulf of California. *Contin. Shelf Res.*, **7,** 715–733.

Roden, G., 1964 Oceanographic aspects of the Gulf of California. *Marine Geology of the Gulf of California,* T.H. van Andel and G.G. Shor, Eds., Vol. 3, *Memoirs of the American Association of Petroleum Geologists*, American Association of Petroleum Geologists, 30–58.

Zavala, J.G., 1993: Parametrización de la fricción lineal de fondo para el Golfo de California mediante la comparación de dos modelos de marea. B.S. thesis, Universidad Autómona de Baja California, 40 pp.